Coupled CFD-MBD numerical modeling of a mechanically coupled WEC array

Xiang Li [a], Qing Xiao [a,*], Yang Zhou [a], Dezhi Ning [b], Atilla Incecik [a], Ryan Nicoll [c], Anthony McDonald [d], David Campbell [e]

[a] Department of Naval Architecture, Ocean and Marine Engineering, University of Strathclyde, Glasgow, G4 0LZ, UK
[b] State Key Laboratory of Coastal and Offshore Engineering, Dalian University of Technology, Dalian, 116024, China
[c] Dynamic Systems Analysis Ltd, 201-754 Broughton Street, Victoria, BC, V8W 1E1, Canada
[d] Industrial Doctoral Centre for Offshore Renewable Energy, Edinburgh, EH9 3FB, UK
[e] Albatern Ltd, Midlothian Innovation Centre, Pentlandfield, Roslin Midlothian, EH25 9RE, UK

ABSTRACT

The development of new wave energy devices (WECs) has continued unabated over the past decades. For large-scale applications, integrating individual WEC into an array system (WEC net) requires considerable expertise and research due to its highly complex and interrelated nature. Often for a WEC net, it contains main structures and multiple sub-structures. The WEC net response is defined as the total responses from all sub-structures, which is highly complex and closely interconnected with each other. This paper aims to develop a fully-coupled numerical modeling tool that can cope with the wave-structure interaction as well as the *mechanical interaction* among each sub-structure in a WEC net. The fluid field is solved by a Computational Fluid Dynamic (CFD) solver coupled with a Multi-body Dynamic structural solver. The hydrodynamic and power take-off performance of Albatern 12S Squid WEC net is studied and the results are validated against available laboratory testing data, and commercial mooring and hydrodynamics analysis software.

It is found that the motion response of the CFD and experimental approach is in close agreement with each other. The interaction force among sub-structures can be well captured, and the results indicate that the mode response of individual float is strongly affected by the mechanical linking-arms as well as the incident wave conditions, which is hard to achieve without such integrated CFD tool. The power take-off (PTO) is modeled using a damping system. The predicted peak output power is found to increase with the decreasing of wave period and an optimal device's damping to reach a maximum power capture exists, which is dependent on the incoming wave period and height.

1. Introduction

To extract energy from the ocean, many wave energy converters (WECs) have been developed in the last decade. Despite the large variation in designs and concepts, WECs can be generally classified into three predominant types, e.g. attenuator, terminator and point absorber (Drew et al., 2009). Attenuators are usually designed to be relatively long in length with multiple mechanical floating segments, which are aligned with the direction the ocean wave propagates in. A typical example is *Pelamis* by Ocean Power Delivery Ltd. (Yemm et al., 2000). The relative displacement between adjacent elements is used to convert the ocean wave energy into electrical power via the hydraulic motor and

generator. In contrast, terminators are deployed with their orientations perpendicular to the direction of the travelling wave. Ocean wave's movement is hindered by terminators and the resulting wave energy is transformed into stored power. Among this type of WEC, Oscillating Water Column (OWC) (Zheng et al., 2020) and Overtopping Devices (OTD) (Cappietti et al., 2018; Liu et al., 2017b)are widely studied. Compared to the above two types, the Point Absorber WEC holds a simpler structure comprising of one float and mooring. It is not sensitive to the wave direction due to its small dimension (Shadman et al., 2018).

In practical applications, it is very common to deploy many individual WEC as an array in order to satisfy a large amount of power take-off requirement. Research conducted of the WECs using numerical

modeling is often the top methods used to uncover insights into the hydrodynamic performance and increase the power production in the design process. However, the method is still relatively undeveloped and requires validation using the results from physical devices. One of the most popular methods for the study of WEC array is the Boundary Element Method, based on the potential flow theory, assuming that the flow is irrotational and inviscid. Therefore, the governing equation is reduced to Laplacian equation for it to function. The wave-air free surface equation is linearized at the time-mean surface position. Lee et al. investigated a multi-body hydrodynamics for a WEC array integrated into a hybrid platform (Lee et al., 2018), in which the interaction effect of the array configuration on the extracted power was studied. They found that the multiple array configuration increases the power capture of the WEC system, while the heave response of the platform is only slightly influenced by the PTO damping force. Ning et al. (2018) studied a hybrid system consisting of an oscillating buoy WEC array and a fixed rear pontoon. It was found that the standing waves formed in front of the pontoon are not beneficial to the energy extraction of WECs, thus leads to a smaller power capture, especially in the high-frequency range. These two studies are all based on a linear potential flow theory in the frequency domain. The dynamic response is estimated by the WEC motion equation and the output power is estimated by the linear PTO damping model.

In addition to frequency domain method, a more complex time-domain analysis is also able to estimate damping parameters of the PTO system. In addition, the later can better predict the performance of WECs via more detailed investigations on transient/unsteady wave-structure-interaction phenomena by including the nonlinear dynamic moorings (Folley et al., 2012). Chandrasekaran and Sricharan performed a numerical study on a novel wave energy converter with multiple floats both in frequency-domain and time-domain with linear PTO model adopted in the software named WEC-SIM (Chandrasekaran and Sricharan, 2020). The influence of the PTO system on the power output is investigated via optimization of the damping coefficients. Although it is found a frequency domain analysis overestimates the results as compared to those obtained from time-domain. Rollano et al. estimated the power extracted by a Floating-Point Absorber (FPA) array with different climates using WEC-SIM (Lawson et al., 2014) (Ticona Rollano et al., 2020). In their study, the fluid-structure interaction was solved using a one-way coupling, in which only the impact of wave on the structure is considered. The power output is found to be dependent on the wave condition in different seasons. The performance is better in winter months compared with summer months.

Due to the limitation of linearization and potential flow hypothesis, the challenge arises in capturing an accurate flow field, when the nonlinear phenomena become significant, which in turn affects the accurate calculation of motion response and power capture. To overcome this issue, several nonlinear models with higher-order accuracy have been developed for WEC studies (Davidson and Costello, 2020), such as higher-order boundary element method (HOBEM) (Ning et al., 2015) and higher-order spectral method (HOS) (Van Rees et al., 2011). Numerical modeling based on a Computational Fluid Dynamics (CFD) method is highly suitable to investigate such problems, in which localized viscous and vortex effects can be examined. It is based on solving

(a) Single float
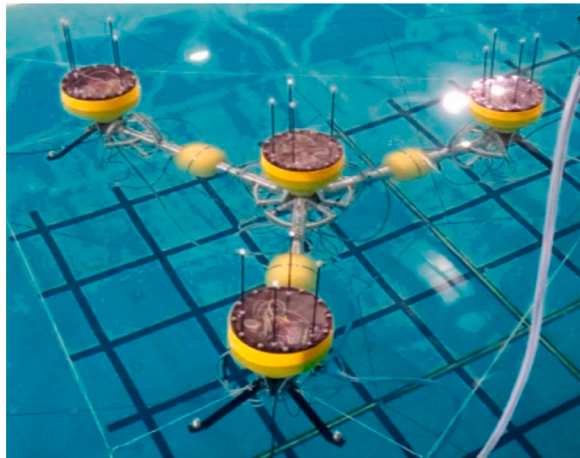
(b) Squid WEC array with sub-structures
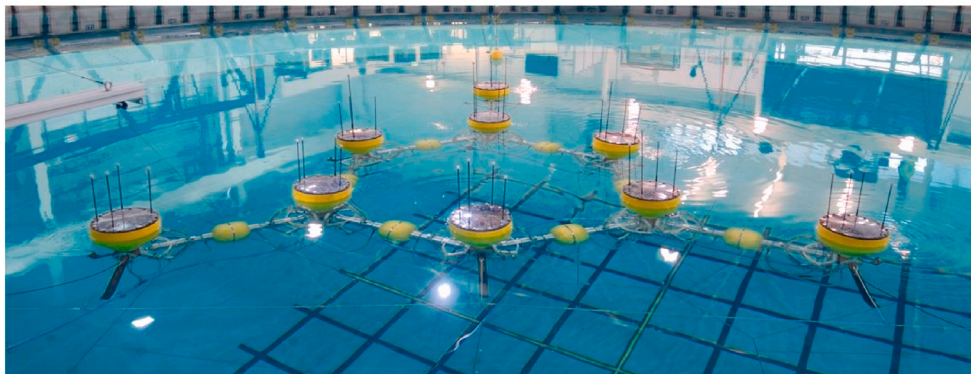
(c) Hex WEC array with sub-structures

Fig. 1. Sketch of the Albatern squid WEC laboratory testing model (Mcdonald et al., 2017).

fully nonlinear Navier-Stokes equations and rapidly developed with its application in numerical modeling of WECs (Agamloh et al., 2008; Chen et al., 2017; Devolder et al., 2018). In the study of Chen et al. (2017), the dynamic response of a point absorbing WEC with a stroke control system is examined. It is revealed that the differences in the WEC behavior predicted by a potential flow theory and a CFD simulation can be significant and vary considerably, depending on ocean wave height.

It is also worth mentioning that, in the above studies, there is no mechanical connection among individual WEC in the array. In practical applications, single WEC is sometimes connected with various mechanical components, such as the sea trail tested devices. One of the typical exemplars is Albatern Wavenet WEC shown in Fig. 1(b) and (c). The multi-segments and the articulation linking arms in the design of such device make up the WEC as a multibody system with mechanical interactions between each section. The interconnected rigid or flexible bodies may also undergo large translational and rotational displacement and motion. This specific feature of the system increases the numerical modeling challenges, which requires a powerful multi-body dynamic solver to be incorporated with a flow solver.

There have been several experiments conducted for WECs with mechanical components (Dang et al., 2019; Ning et al., 2016; Zurkinden et al., 2014). Meanwhile, limited studies are found focusing on the mechanical-wave-structure system issues, especially for numerical studies. Using a frequency domain method, Zhang et al. investigated the performance of a two-body articulated Eagle wave energy device (Chao et al., 2018). The mechanical external damping was studied in a wide wave frequency range in order to optimize the power output. The most dangerous wave angular frequency ranging from 0.2 to 0.5 rad/s was identified, with which excessive movement occurs, causing the damage of the device. Although the frequency method can obtain the dynamic response by motion equations in the post-processing process, it can only be a rough estimation of the floating structure. Yu et al. developed a module in WEC-SIM which can model a WEC's conversion of mechanical power to electrical power through its PTO (So et al., 2015). The performance of the RM3 floating point absorber with two different PTO systems was evaluated. Their results showed that the direct-drive system is more efficient as compared to the hydraulic system, but the latter can obtain smoother power output. A more complex WEC system, e.g. ALETTONE, which consists of a 4-bar linkage and a floating plate was developed in the work of Albert et al. (2017). The multibody WEC was simulated using SimMechanics and the hydrodynamic force was addressed by an impulse response function, which was calculated separately from ANSYS/AQWA.

On large multibody WEC system with mechanical connection, few studies can be found. Chandrasekaran studied the performance and optimization of a bean-shaped multi-body floating WEC using WEC-SIM (Chandrasekaran and Sricharan, 2021; Sricharan and Chandrasekaran, 2021). The performance of WEC with different number of components are studied, together with the PTO damping in which a real-time simulation is achieved. It is found that WEC-SIM can obtain reasonably good results comparable to CFD results with moderate sea states. However, for more extreme sea states, the linear-based results have significant errors (van Rij et al., 2019). This is because the higher-order non-linear effects is excluded in WEC-SIM. Therefore, the motion of WECs with strong resonance motion may be under-estimated due to the linearized free-surface assumption. In the comparison conducted by van Rij et al., WEC-SIM results show much smaller sway drift and yaw motion than CFD results (van Rij et al., 2019).

As far as the authors understand, none of the existing commercial CFD software packages can study the hydrodynamic performance of a rather complex mechanical system, as the wave net studied in this paper, illustrated by Fig. 1 comprising a great deal of mutually influenced substructures and restraints. For the Hex WEC system studied in this paper shown in Fig. 1(c), the mechanical system includes up to eighteen mutually interacting sub-components such as floats and linking-arms, and articulations connecting them with Power Take-off (PTO) and

mooring system.

In the present study, an integrated numerical modeling tool is developed, to study complex mechanical system interaction with waves. Challenges arises when solving such large systems in the past studies, especially for the closed-loop mechanical system presented in this paper. To deal with this systematic problem, a high fidelity CFD solver is fully coupled with a multibody dynamics (MBD) tool. The later method studies the dynamic behavior of multiple interconnected rigid or flexible bodies and are widely used in robotics and vehicle dynamics (Eich-Soellner and Führer, 1998; Shabana, 1997). With this tool, the motion responses and mechanical connection force between individual floats and linking-arms can be fully resolved simultaneously with any arbitrary topological complexity. The detailed data provided can be used for the prediction of the weakest mechanical component in the WEC net, where the peak mechanical force may occur and thus become the most vulnerable part in the system. This is believed extremely helpful to guide the industry design for complex WEC net.

2. Numerical methods

In this study, the WEC net system is affected by a variety of factors, thus a fully coupled Fluid-structure-interaction (FSI) tool is used to solve this problem. Particularly, a CFD solver is used to generate waves and to compute the flow field around the structures. A multi-body dynamic code MBDyn (Masarati et al., 2014) is added to compute the dynamic response of the WEC under wave conditions taking into account the force and damping impact from the connecting rods in the WEC net. A coupling code is developed to achieve the data exchange and handle the moving CFD mesh between the above two solvers.

2.1. Flow solving

The simulation of fluid flow problem in the WECs FSI problem is performed based on the open-source CFD toolbox OpenFOAM. The developed solver is based on the multi-phase flow solver interFoam. In this model, the flow is assumed to be incompressible and viscous which is governed by the continuity equations and incompressible Navier-Stokes equations:

$$\nabla \cdot U = 0 \tag{1}$$

$$\frac{\partial \rho U}{\partial t} + \nabla \cdot \left(\rho \left(U - U_g \right) U \right) = -\nabla P_d - g \cdot x \nabla \rho + \nabla \left(\mu_{eff} \nabla U \right) + (\nabla U) \cdot \mu_{eff} + f_\sigma \tag{2}$$

where U is the velocity of the fluid and ρ is the density. U_g denotes the speed of the motion of the mesh grid. P_d denotes the dynamic pressure. g is the gravity acceleration. μ_{eff} denotes the effective dynamic viscosity, f_σ is the surface tension which is only considered on the free surface.

The Volume of Fluid (VOF) method (Hirt and Nichols, 1981) is used to capture the free surface. The volume fraction α is used to govern the interface of air and water. $\alpha = 1$ in the water phase and $\alpha = 0$ in the air phase. The volume fraction is governed by the following transport equations:

$$\frac{\partial \alpha}{\partial t} + \nabla \cdot \left(\left(U - U_g \right) \alpha \right) + \nabla \cdot \left(U_r (1 - \alpha) \alpha \right) = 0. \tag{3}$$

where Ur is the velocity field to compress the interface as the compression velocity.

In the multi-phase flow problem, fluid density and viscosity can be written as a mixture of water and air:

$$\rho = \alpha \rho_w + (1 - \alpha) \rho_\alpha \tag{4}$$

$$\mu = \alpha \mu_w + (1 - \alpha) \mu_\alpha \tag{5}$$

where ρ_w and ρ_a denote the density of water and air, μ_w and μ_a denote the

viscosity coefficient of water and air.

To generate waves, an in-house code is applied to the OpenFOAM toolbox. In this tool, the incident waves are generated by specifying free surface elevation and velocity distribution at the inlet boundary. This method has been proven to be very effective in previous studies (Liu et al., 2017a). In this study, Stokes 2nd order wave theory is applied to represent the incident wave, where free-surface elevation can be defined as:

$$\eta = \frac{H}{2}\cos\theta + \frac{H}{8}\left(\frac{\pi H}{L}\right)\frac{\cos kd}{\sinh^3 kd}(\cos 2\,kd + 2)\cos 2\,\theta. \tag{6}$$

where H and T denote the wave height and wave period, k and d denote wave number and water depth, θ is the phase.

The fluid velocity at the inlet boundary thus can be given as the following:

$$u = \frac{\pi H}{T}\frac{\cos k(z+d)}{\sinh kd}\cos\theta + \frac{3\pi H}{4T}\left(\frac{\pi H}{L}\right)\frac{\cos 2\,k(z+d)}{\sinh^4 kd}\cos 2\,\theta. \tag{7}$$

$$w = \frac{\pi H}{T}\frac{\sinh k(z+d)}{\sinh kd}\cos\theta + \frac{3\pi H}{4T}\left(\frac{\pi H}{L}\right)\frac{\sinh 2\,k(z+d)}{\sinh^4 kd}\sin 2\,\theta. \tag{8}$$

To reduce wave reflection at the outlet boundary, a wave damping scheme is integrated into the present model (Wang et al., 2021), in which the sponge layer is used to damping waves and takes effect by adding an additional artificial viscous term as a source term to Eq. (2). The new term is defined as

$$f_s = -\rho\mu_s U. \tag{9}$$

where μ_s is the artificial viscosity coefficient calculated by the following equation:

$$\mu_s(x) = \begin{cases} \alpha_s\left(\dfrac{x-x_0}{L_s}\right)^2, x > x_0 \\ 0 \quad, x \le x_0 \end{cases}. \tag{10}$$

where α_s defines the damping strength for the sponge layer, x_0 and L represent the start position and length of the sponge layer.

2.2. Multibody interaction solver

Generally, a multibody system is defined as a complex system consisting of more than one rigid body, where each body can interact with others. This is exactly the same situation as for our WEC array, where the floats are the main components and the linking arms are sub-structures to connect them (see Fig. 1(a) and (b)). There are articulations at the connection points between the two floats, imposing constraints where rotation mode is permitted while translation is prevented. At the articulations, damping or stiffness can be applied if the electric damping of the joint is numerically modeled. The mooring lines are used as a practical solution to restrain the WEC system from drifting caused by the wave and current. This constraint is modeled by the force with specified constitutive law numerically. In the present study, the dynamics of such a complex system is solved by MBDyn (Ghiringhelli et al., 2000).

MBDyn adopts a Lagrange multiplier or redundant coordinate set formulation for a multibody system. Compared to the reduced coordinate set method, where only minimum numbers of degrees of freedom (DoFs) are used to describe the motion of the system, a redundant formulation which allows 6 DoFs motion for each body and constraints are enforced by Lagrange multipliers (Masarati and Sitaraman, 2011).

For each body of the system, Newton-Euler equations of motion are established in the differential-algebraic form as a set of first-order equations together with the constraint equation, resulting in a system of Differential-Algebraic Equations (DAE) as follows:

$$M\dot{x} = p. \tag{11}$$

$$\dot{p} + \varphi_x^T\lambda = f(x, \dot{x}, t). \tag{12}$$

$$\varphi(x, t) = 0. \tag{13}$$

where M denotes the inertia matrix of the rigid body, x denotes the translational and rotational parameters in the global reference frame. p refers to the momentum of the body. λ denotes the vector of the Lagrange multipliers for the constraints; f is the external force and moment vector exerted upon the body which might be related to its displacement and velocity as well as time. φ is a set of kinematic constraints applied on the body and φ_x^T is the Jacobian of φ with respect to the generalized coordinates. At the conjunction of the arm and float, the constraint should be applied acting as a spherical joint, which is shown in Fig. 2. The joint connects two objects like a hinge, each object owns six degrees of freedom and moves freely, but their relative translational displacement is restrained. Only relative rotation is allowed.

Constraint equations φ are as follows:

$$\varphi(x(t)) = (x_2 + b_2) - (x_1 + b_1). \tag{14}$$

$$b_1 = R_1\vec{b}_1, b_2 = R_1\vec{b}_2. \tag{15}$$

where $\vec{b}_1$ and $\vec{b}_2$ are the offset of connection point from structure 1 and 2 in structure reference, R_1 and R_2 are the orientation of the structures.

When electric damping is applied onto the spherical joint, it creates a damping torque $\tau_i(t)$, this can be quantified by Equation (16), where i denotes the number of the floats, β denotes the electric damping and ω denotes the rotational angular velocity. The total power output of the WEC net can be estimated by Equation (17)

$$\tau_i(t) = \beta\omega(t) \tag{16}$$

$$W(t) = \sum_{i=1}^{9}\tau_i(t)\cdot\omega(t) \tag{17}$$

To simplify the complexity of the system, the mooring which controls the drifting motion is substituted with a force between two points. Mass
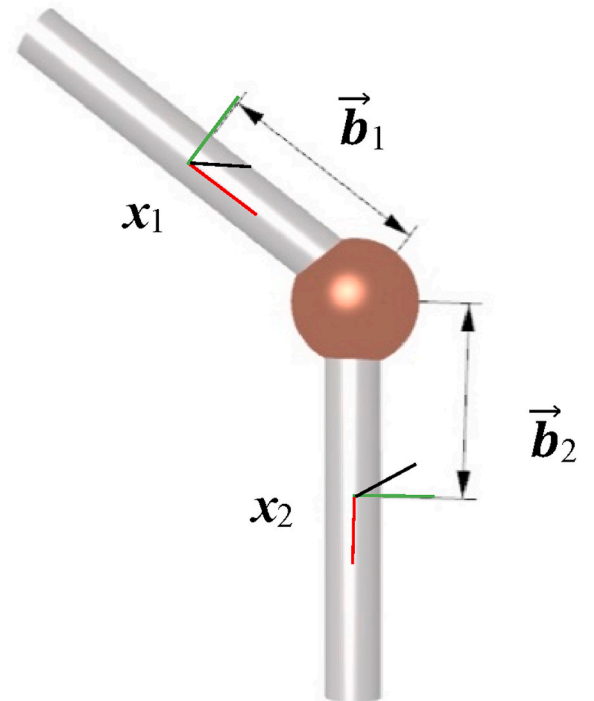

Fig. 2. Sketch of the spherical joint.

of ropes is neglected in our model, reducing the simulation time significantly. The force of the rope depends on the relative distance between the two points, which follows the following constitutive law:

$$f = \begin{cases} k \cdot \varepsilon (\varepsilon > 0) \\ 0 (\varepsilon < 0) \end{cases}. \tag{18}$$

where k is the stiffness of the ropes, ε is the strain of the ropes. The force only exists when the ropes are elongated ($\varepsilon > 0$).

2.3. Data transfer

After receiving the dynamic response of the structures, the data should be transferred back to the CFD solver. The coupling method between the CFD solver and MBDyn software was previously implemented and utilized to solve a flexible wind turbine blade analysis, in which the blade was simplified as a beam-like structure in the structural solver (Liu et al., 2019).

The coupling strategy performed in the present study for a WEC net is shown in Fig. 3. The CFD solver and the structural solver run simultaneously at separate computer processes and the data exchange is achieved with the help of TCP/IP protocol. At the very beginning of the simulation, MBDyn uses a TCP/IP socket for two-way communication to exchange information with the CFD solver. The hydrodynamic force on the components calculated from the CFD solver, is transferred into the multi-body system solver, MBDyn. By accepting the force data, MBDyn predicts the dynamic response of the WEC system and then feeds the updated position data back into the CFD solver. The CFD mesh is then updated, followed up by an update of the entire flow field. The communication between the two solvers is completed at each iteration in each time step so that strong coupling is achieved with a robust and fast convergence.

3. Problem statement

3.1. Squid WEC

The Squid WEC array in this study is a geometrically simplified version of the Squid WEC system from Albatern Ltd. (Mcdonald et al., 2017). There are two WEC arrays examined in this study, one consisting of 4 floats, and another having 9 floats as displayed in Fig. 1 (b) and (c). The Squid model in Fig. 1 is a 1:18 Froude scaled physical model which was tested in the FloWave Ocean Energy Research Facility in Edinburgh. The hull of each float is made up of upper and lower cylinders, with a cone-shaped transition in the middle (see Fig. 1(a)). These floats are connected by several linking arms to form a WEC net. There's a buoy at the center of each arm to offset the arm weight. The angle between the arms is 120°. At the connection points between the arms and the floats, articulations are installed which can be equivalent to universal joints, allowing the free rotation of each node. The energy conversion is achieved via the relative rotational motion between the floats and linking arms. The mooring grid with a constant stiffness is used at the outer loop of the array to control the drift of the system.

3.2. Numerical WEC model parameters

To reduce the complexity of the system from the perspective of CFD simulation, the model described above is simplified in the CFD model shown in Fig. 4. Geometrical dimensions of the array are as follows: the height of the single float is 9.0 m, the diameter of the upper and lower cylinder is 6.5 m and 1.6 m and the length of the arm is 20.754 m. Both the floats and the linking arms are rigid bodies, thus no deformation is allowed. The arms are modeled as long cylinders without buoyancy, and adopted a smaller mass compared to the mass of floats. No hydrodynamic forces on the arms are calculated. The articulations at the ends of arms are achieved by using a spherical joint constraint, as described in section 2.2. The mooring grid is simplified without considering the circular grid at the outer loop. The far ends of the mooring grid are fixed in space and the mass of the grid is disregarded. The incident waves come from the left and the static water depth is 63 m.

The boundary conditions and dimensions of the computational domain are shown in Fig. 5. At the inlet boundary, the flow field is prescribed based on the Stokes 2nd order wave theory as mentioned previously in Section 2.1. The pressure gradient is set to zero. The outlet boundary is treated as a zero-gradient boundary for the pressure while
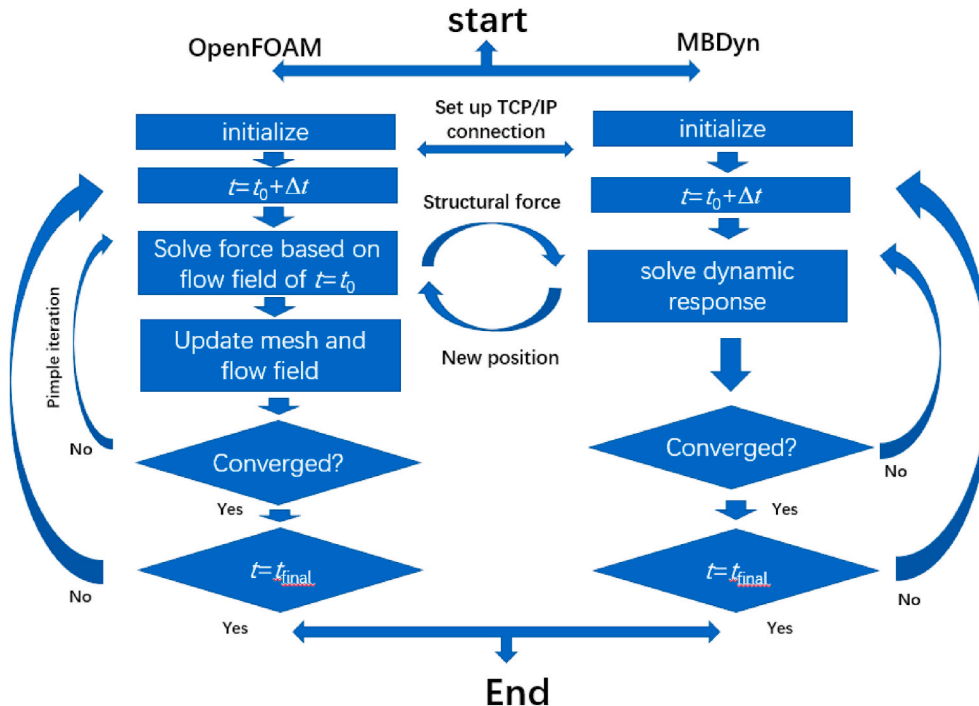

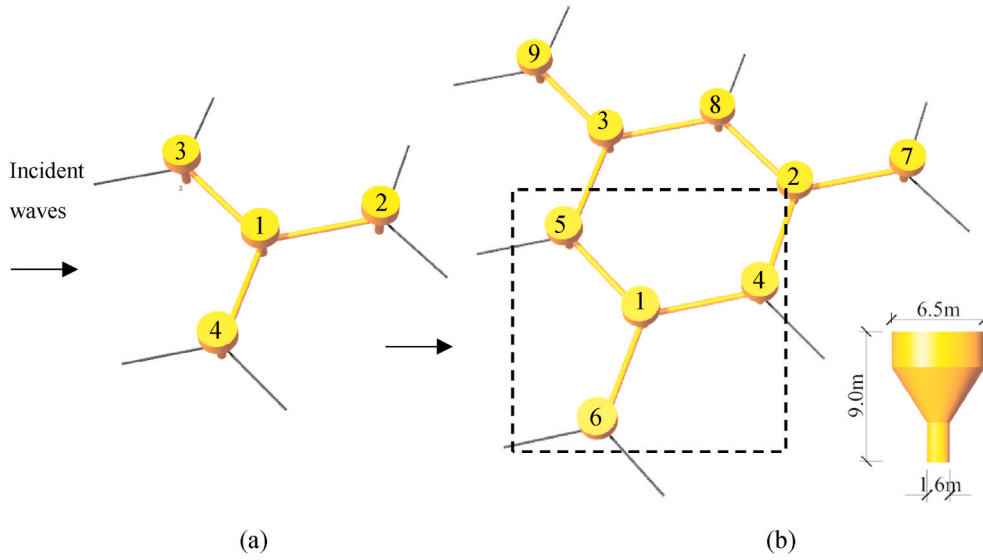**Fig. 3.** The workflow of the coupling strategy.

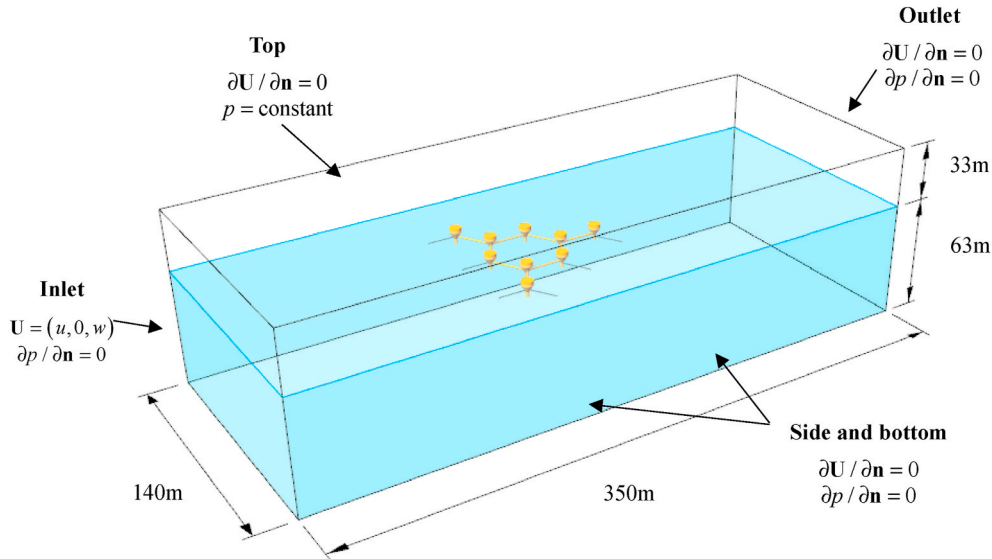**Fig. 4.** Sketch of the CFD model for (a) 4-node array (b) 9-node array.

Fig. 5. Dimensions and boundary conditions for the WECs simulation.

the velocity is fixed as zero when the relaxation zone is applied. The top is treated as a constant pressure inlet/outlet which represents the atmosphere. Both the bottom and side boundaries are set as wall boundary conditions. On the hull of the nodes, a non-slip wall boundary condition with zero pressure gradient is defined. The dimension of the domain of the full-scaled model is -150 m $\leq$ X $\leq$ 200 m, -70 m $\leq$ Y $\leq$ 70 m, -63 m $\leq$ Z $\leq$ 33 m. The origin of the coordinate system is located on the static free surface at the horizontal center of the array. The side boundary is set far enough from the structures to avoid the impacts of walls. The relaxation zone is set close to the outlet boundary with a length of about one wavelength. Although it is recommended to use a relaxation zone of two wavelength, in our numerical wake tank testing, we found that one wavelength is sufficient to suppress the free surface. To reduce the overall computational cost, one wavelength relaxation zone is adopted. To model WEC hydrodynamic responses, laminar flow is assumed in this study. This is widely accepted by researchers because it was found that there is no apparent disparity between the results obtained from turbulence or laminar models when the flow is mainly dominated by wave rather than current (Finnegan and Goggins, 2012; Wang et al., 2021).

3.3. CFD configuration

Because the structures are not fixed and the position of WEC may change with time, moving CFD mesh is required. Three-dimensional unstructured meshes consisting of hexahedra (hex) and split-hexahedra (split-hex) elements are generated with the built-in meshing tool SnappyHexMesh in OpenFOAM. The mesh refinement is achieved near the free surface as shown in Fig. 6 (a). According to the Stokes wave theory from equations (7) and (8), the wave motion only affects the fluid near the free surface. Therefore, mesh size far from the surface layer can be set larger to speed up overall computational time. Meanwhile, the free surface region within a height of one wave height (H) should be refined to achieve accurate results. Particularly, in this study, the cell sizes around the surface layer satisfy $\triangle z = H/10$. Along x-direction, the grid size satisfies $\triangle x \leq \lambda/60$, where λ is the wavelength. Apart from the free-surface area, the mesh around the WEC nodes is also refined as plotted in Fig. 6 (b).

In the present study, PIMPLE (a combination of Pressure Implicit with Splitting of Operator (PISO) and Semi-Implicit Method for
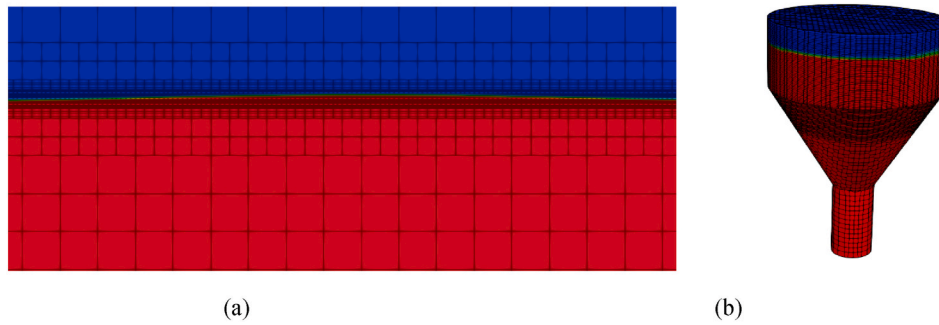
Fig. 6. Mesh refinement (a) near the free surface (b) on the WEC node.

Pressure-Linked Equations (SIMPLE)) algorithm is utilized to solve the pressure-velocity coupling. A second-order Crank-Nicolson scheme is used for temporal discretization. A second-order upwind scheme is adopted for convective terms. Gradient terms are handled via a second-order cell-limited Gauss linear scheme (Mcdonald et al., 2017). Four multistep integration schemes can be chosen in MBDyn, among which the Crank-Nicolson method is used in this study. For the computation of linear systems and nonlinear problems, a linear solver called "umfpack" and a Newton Raphson scheme are chosen respectively (Masarati, 2017). The timestep must be set the same as that in the CFD solver for data transfer.

3.4. Nonlinear Morison ProteusDS model configuration

ProteusDS is a commercial software program that solves multi-body system response in wind, waves, and currents. It is often used for mooring and marine operation analysis for marine renewable energy systems, including wave and tidal systems. To design a mooring system for a renewable energy system, dozens or even hundreds of simulations must be completed in a wide range of ocean conditions. This means a practical approach in modelling the system response may be necessary. A balance of accuracy for computational execution speed may be critical to ensure practical design of mooring systems for WECs.

Because the Squid WEC uses a distributed network of smaller floats to generate power, it lends itself to the use of a nonlinear Morison model to compute the system motion. While wave radiation and diffraction effects are often important, but become less so when the incident wavelengths are large compared to the individual structures in the system. An equivalent numerical model of the Squid WEC arrange was configured in ProteusDS, using the nonlinear Morison model for the floats and articulated connections of the network for the purposes of comparison to the CFD results. The wave radiation and diffraction effects in the nonlinear Morison model were neglected. The nonlinear Morison model in ProteusDS accounts for the incident wave excitation force, drag, and added mass effects based on the wetted hull of each float (Nicoll et al., 2012). The comparison between the nonlinear Morison ProteusDS model and CFD results illustrate and inform the trade-off of numerical accuracy and computational efficiency between the methods.

4. Results

4.1. Verification and validation on a 4-node WEC array

The developed CFD approach is first compared with the experimental testing results for validation (Mcdonald et al., 2017) on a 4-node WEC array. The wave parameters used in the simulation are shown in Table 1. In the experiment, the joints connecting the arms and floats are not ideal, leading to the large friction and resistance appearance at the joint, thus moderate the amplitude of rotation significantly. A numerical test on the influence of friction on the dynamic motion of WEC shows that it can lower the pitch amplitude significantly in some conditions. The

Table 1
Wave parameters for cases 1-4.

	Wave height H/m	Wave period T/s	Water depth h/m
Case 1	1.5	9.5	63
Case 2	1.5	10.5	63
Case 3	1.0	9.5	63
Case 4	1.0	10.5	63

experimental test is conducted on this 4-node WEC full-scale model to obtain the linear friction coefficient. The maximum torque caused by the friction is 283kNm. Therefore, this data is directly used in the numerical study, to simulate the contribution of friction.

A sensitivity study of mesh density and the unsteady time step is conducted. Fig. 7 shows the time history of wave amplitude in the middle of Node 3 and Node 4 with different mesh densities and time steps. The numbers of cells are 2.6 million (fine mesh), 1.9 million (intermediate mesh), and 1.0 million (coarse mesh). For the results with different time steps, the predicted wave amplitude hardly changes when $\triangle t < 0.005$s. Considering the cost of computational time, a time step of $\triangle t = 0.005$s is chosen for the CFD modeling in this study. Similarly, a mesh of intermediate density is chosen. In a 9-node case, the intermediate mesh consists of 2.4 M cells and a time step of $\triangle t = 0.005$ is chosen. Simulations are performed on the Cirrus UK National Tier-2 High Performance Computing (HPC) facility at EPCC with 3 compute nodes, each of which contains two 2.1 GHz, 18-core Intel Xeon E5-2695 (Broadwell) series processors. The overall time for a typical 4-node case is approximately 23 h, which may increase for a 9-node case.

Fig. 8 shows a typical free surface elevation variation for case 1 between $t = 110$s–120s within one wave period. As seen from the figure, a clear dynamic motion response of floats is well captured with the incident wave propagates. In addition, the diffraction and wave run-ups can be observed around each float. It is noted that the dominant motion mode comes from pitch, and the motion trajectory is very similar for all three nodes both in CFD and experimental results, thus, only the result of node 2 is compared with experimental data in Fig. 9. The six blue points in Fig. 9 (a) are the instantaneous time indicated in Fig. 8.

As we can see from Fig. 9, the two results appear similar in terms of the phase and amplitude although the CFD results display more periodic results than the experimental results, especially at the trough of curves. This may be due to the simplified details of our CFD model. For instance, the articulation attached to the nodes is simply represented as the joint with certain values of damping and stiffness, without physical presence. As such, their blockage effect on the fluid flow is absent in our simulation. In addition, the simplification of the linking arms can be another possible reason.

The heave mode of WEC is not directly compared between the experiment and CFD because the mooring lines are absent in our CFD model. It is well known that the mooring lines may have some effects on the heave motion of floats. An additional comparison between the CFD model and the nonlinear Morison ProteusDS model is completed for
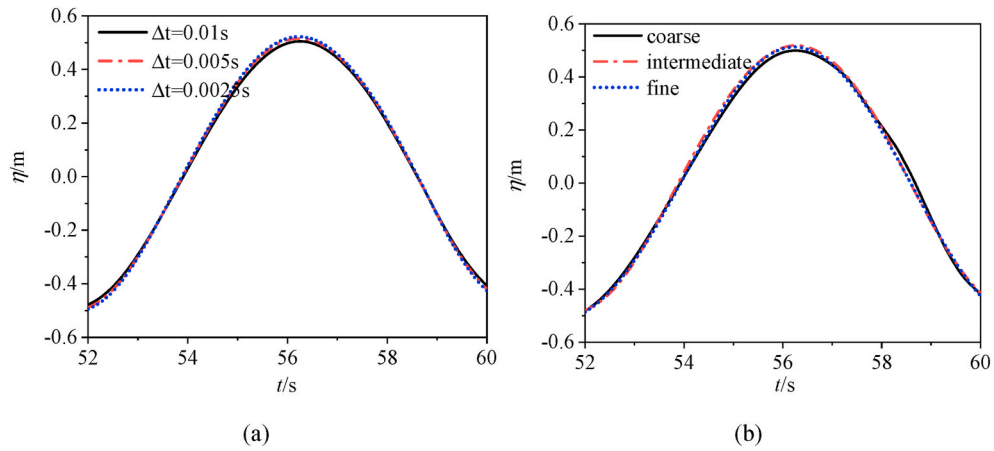
Fig. 7. Time history of surface elevation in the middle of node 3 and 4 for Case 1 of different (a) mesh density (b) time step.
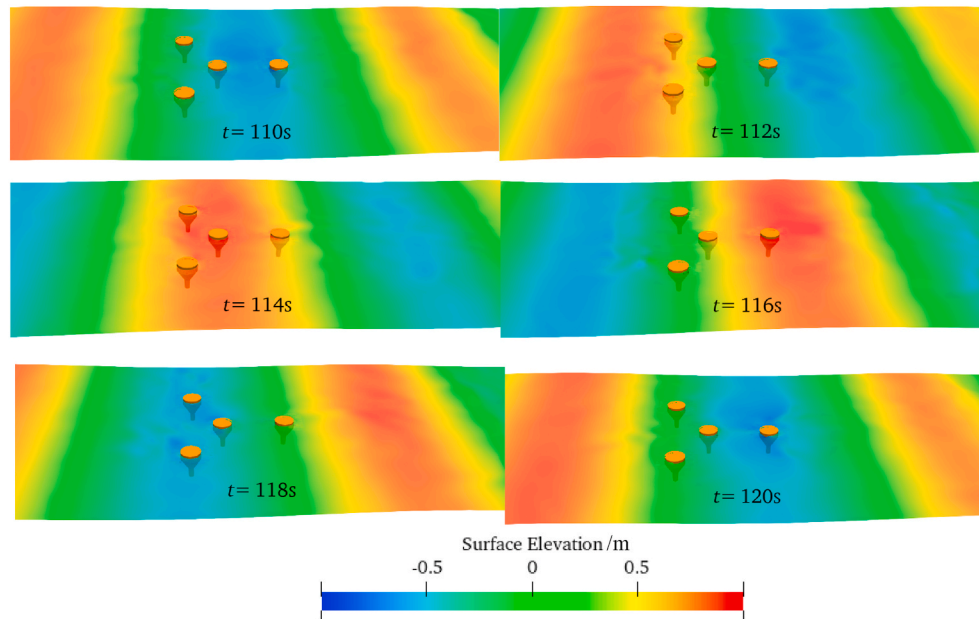

Fig. 8. Contour of the free surface elevation from $t = 110\text{s}–120\text{s}$ with $H = 1.5$ m and $T = 9.5\text{s}$.
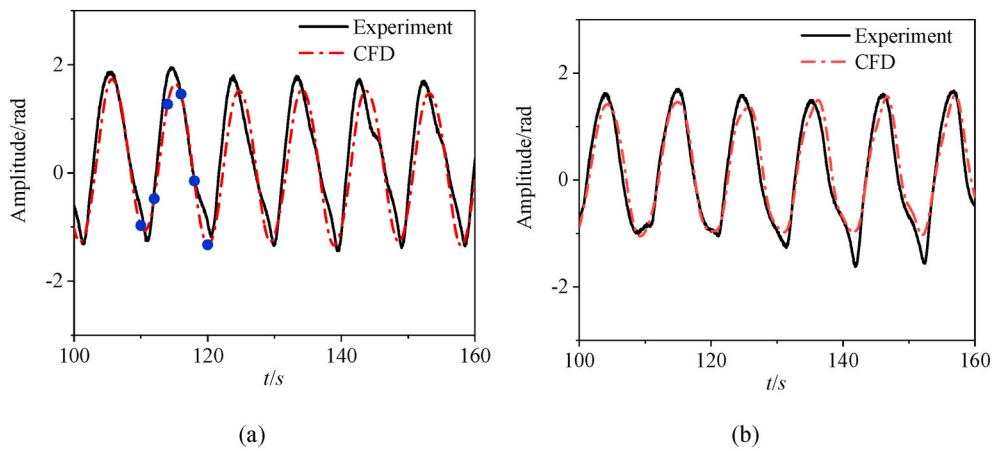

Fig. 9. Pitch motion of node 2 for (a) case 1 (b) case 2. Blue labels are the sampling time shown in Fig. 8. (For interpretation of the references to color in this figure legend, the reader is referred to the Web version of this article.)
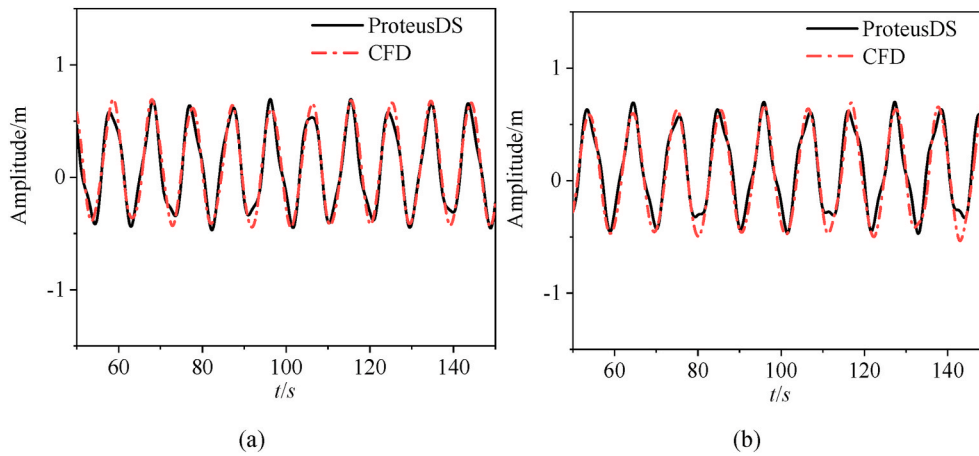
Fig. 10. Heave motion for (a) case 3 (b) case 4.

cases 3 & 4 as shown in Fig. 10. Generally, they are in close agreement although the ProteusDS results are less stable than the CFD results. This may be due to the approximation to resolving viscous in ProteusDS using drag coefficients and relative velocity. This simplified approach does not capture the same level of detail as the CFD results do, including flow separation, skin friction effects, and variation in drag coefficient. The free-surface effect in the nonlinear Morison ProteusDS model can account for variation in wetted area of the float hulls, but it does not account for wave radiation or diffraction loads. These free surface effects are included in the CFD model as well.

Although both results have close agreements in heave response, the comparison in the pitch mode reveals some distinct differences as shown in Fig. 11 for Cases 3 and 4. In particular, the CFD results show larger peaks than that of ProteusDS for both cases. The phase discrepancy between the two results is obvious for Case 3 but reduces for Case 4 with a longer wave period. It is expected that a weak non-linear wave-structure-interaction appears as a consequence of the decreasing of wave steepness in Case 4.

To better understand the nonlinearity in this problem, a Fast Fourier Transform Algorithm (FFT) is applied to the data in Fig. 11, and the results are presented in Fig. 12. Two peak frequencies are observed, the first one is in relation to the incident wave frequency, while the second links to the float natural frequency of vibration. The natural pitch frequency of the float is around 0.15 Hz. Given the first frequency at 0.1 Hz, both the CFD predicted result and nonlinear Morison model result are consistent. However, at the 2nd frequency, the nonlinear Morison model provides a much lower peak than CFD, indicating the appearance of

nonlinearity and its strong impact excited by the waves. This result is expected because the nonlinear Morison model does not account for wave diffraction and interaction between the floats, while the CFD model does. This complex interaction creates an ongoing transient disturbance in the float pitch natural frequency, which is clearly seen more strongly in the nonlinear CFD model. From this perspective, the CFD model has an advantage over the nonlinear Morison model, especially for the cases where there is significant influence induced by the floating structure on the water wave surface. The greater the number of floats, the larger the water surface disturbance and the importance on pitch motion is.

4.2. Dynamic motion of the 9-node array

A more complicated WEC array consisting of 9 nodes is investigated as displayed in Fig. 4 (b). The 9-node array in this case contains far more components and has a centered closed loop, with which the topological complexity and the constraints limiting the individual float degree of freedom motion increase as compared to an open-loop system for 4-node WEC. The study is focused on Case 3 as summarized in Table 1. With the numerical modelling tool developed, either a systematic study of the whole WEC net or a localized analysis of specific single sub-structure/component is possible. To better demonstrate the above features, we will present our results starting with a description on global motion of WEC net followed by the interactions between specific substructures.
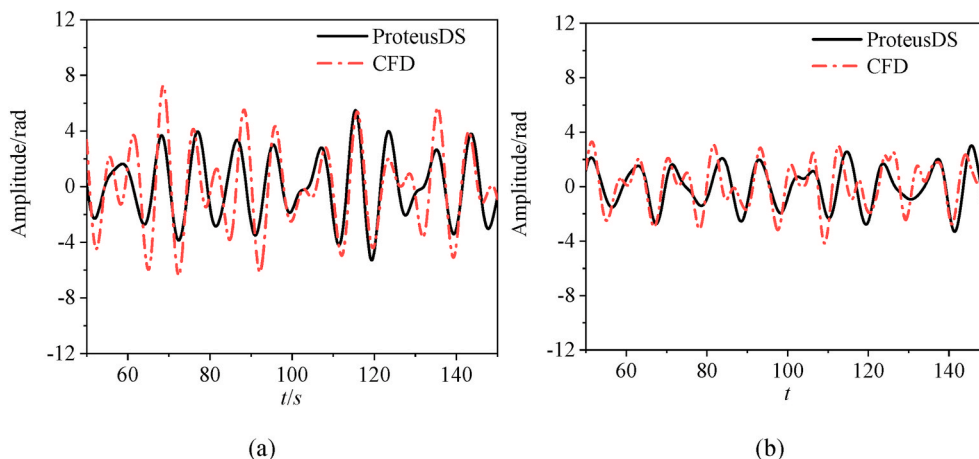

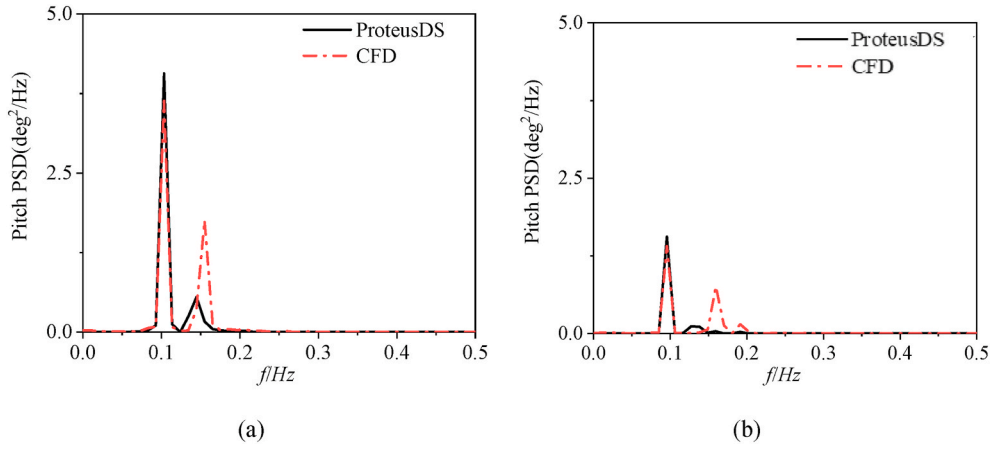**Fig. 11.** Pitch motion for (a) case 3 (b) case 4.

Fig. 12. FFT analysis of the pitch motion for (a) case 3 (b) case 4.
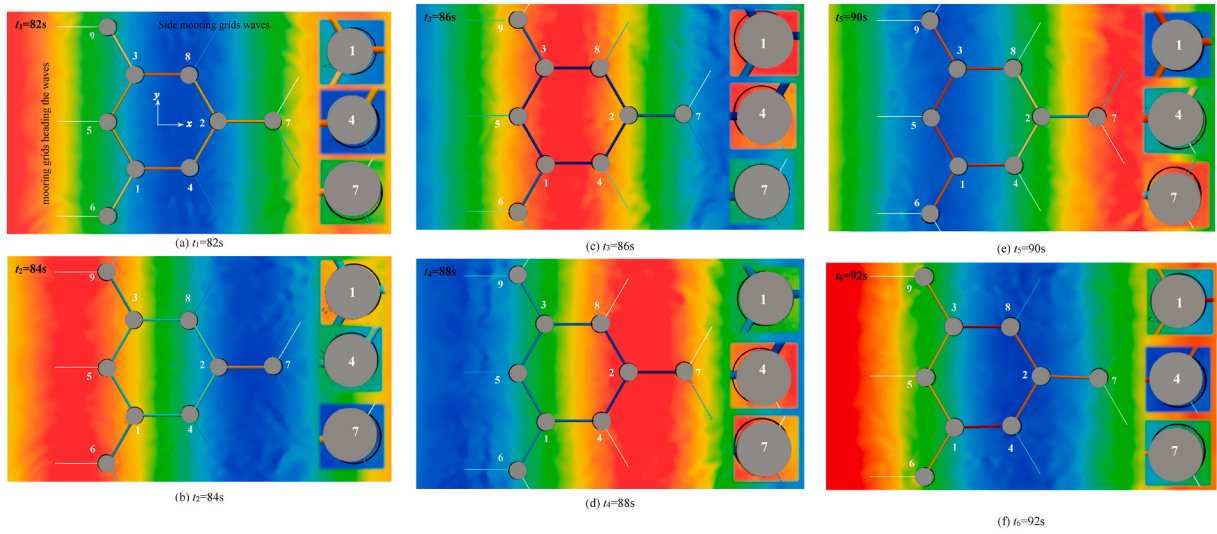

Fig. 13. Free surface elevation for 9-node WEC from $t_1 \sim t_6$ from the top view. The contour on the linking-arms and moorings denotes the axial force, the enlarged figures around node 1, 4 and 7 denote their new position compared to their old position in the last sampling time (black shadow).

4.2.1. Global motion response of WEC net

Fig. 13 shows the free surface elevation from a top view of the WEC net within a wave time period, specifically, from $t_1 = 82s$ to $t_6 = 92s$, including the mechanical linking-arms and mooring grids. The color of arms denotes the CFD predicted axial force along the arms with the contour legend included in the figure. Only tensile force is allowed for the moorings since a mooring grid cannot sustain a compression motion. The 'shadow nodes', i.e. the black circles plotted underneath each node, represent the floats' location at the last sampling time. For ease of description, we define three phases from t_1 to t_3. Phase 1 is named as 'wave trough phase', during which the wave trough is just passing through the WEC array. Phase 2 is called the 'transition phase', when a wave trough (or wave crest) has passed the array, however, the next wave crest (or wave trough) has yet to arrive. Phase 3 is referred to 'wave crest phase', meaning a wave crest has passed the array completely.

As shown from Fig. 13, t_1 is in the 'wave trough phase', the WEC array is moving backward against the wave propagating, indicated by the plot that each node is moving along the negative x-direction. At this moment, the tensile force of the side mooring reaches its maximum to 'drag back' the array to its previous location. Afterward, WEC develops into the 'transition phase' at t_2. It can be inferred from the 'shadow nodes' that, all nodes hardly change their positions along the x-

direction. The axial force of the arm is eased. In the last stage of the 'wave crest phase' at t_3, the WEC array is drifted towards the wave propagation direction, the axial force of arms reaches the negative peaks, indicating these linking arms are stretched. The above phase variations appear periodically within one wave period. It is reasonable to conclude that the compression of the mechanical arms results in the movement of the array backwards, which is associated with the 'wave trough phase'. The situation is observed vice versa in the 'wave crest phase'.

4.2.2. Translational mode response

Apart from the above observations on the global motion of the WEC array, the dynamic response of individual node, i.e. Nodes 1,2,4 and 7 in the net, is discussed in this section. The aim is to demonstrate that the individual nodes behavior and their interaction have impact on the response of WEC net.

The motion trajectories of various nodes in the x-z plane are displayed in Fig. 14, derived within two sampling wave periods. The trajectory of floats follows approximately closed ellipses, with a similar maximum displacement of 0.8 m in x and 1.0 m in the z-direction, respectively. A further examination of Fig. 14 suggests that the trajectories for Node 1 and Node 2 are very similar, i.e., the ellipses lean backward in the negative x-direction, while they appear to be in the
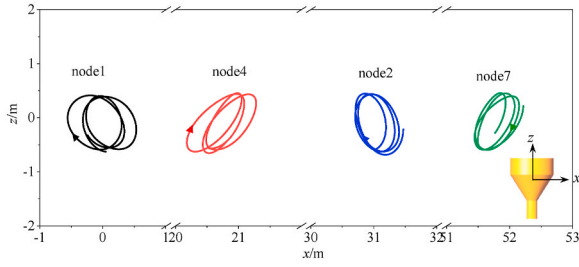
Fig. 14. Motion trajectories of an individual node in an *x*-*z* plane within two wave periods.

Fig. 16. Heave amplitude for individual floats.

positive *x*-direction for Node 4 and 7. This clearly indicates that the motion response for individual float is diverse, depending on their actual position and connection in the WEC net, which is actually induced by the mechanical force generated in the linking arm, discussed in the next part.

Fig. 15 shows the velocity of floats in *x*-direction v_x, the mechanical force acting on the floats along x-axis F_{mx} provided by linking arms and mooring grids, and the total resultant force acting on floats along x-axis F_{tx}. One observation is that F_{tx} is of the same magnitude as F_{mx}, implying that the mechanical components, such as linking arms herein, play a significant role in the motion response of floats. It is known that in this WEC system, the response of mode is determined by a combined input from both hydrodynamic pressure force and the mechanical force generated via mechanically coupled linking arms. Given node 1 and 2 as examples, as shown from an enlarged plot in Fig. 15, the F_{mx} variation is almost coincident with v_x within a wave cycle, indicating that the velocity and mechanical force are pointing in the same direction. However, for Node 4 and 7, the F_{mx} and the v_x are pointing to two opposite directions. The above force and velocity relation lead to two entirely different motion trajectories for Nodes 2,4 and Nodes 4,7 shown in
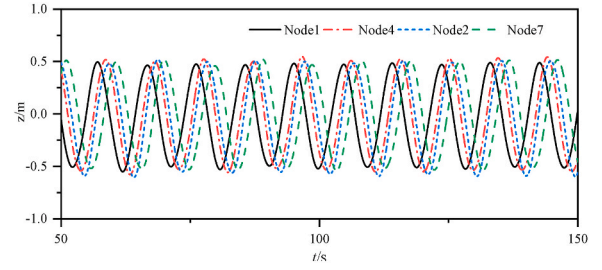
Fig. 14.

The motion in z-direction, namely the heave response history is shown in Fig. 16. Each float heaves up and down with the wave period. The motion amplitude is around 1 m, almost the same as the wave height. It can be observed that the linking arms does not influence the floats motion in the heave direction. This is because the displacement at the two ends of the arm is very small (the maximum relative displacement is 0.5 m), which is immaterial compared to the arm length (20.754 m), thus resulting in a tiny component force in the z-direction.

4.2.3. Rotational mode response

The lateral view of the float's rotational motion at t_1-t_6 is shown in Fig. 17. The color of the floats denotes the surface dynamic pressure distribution. The 'shadow nodes' underneath each node represent their positions at the last sampling time. It can be seen that the magnitude of the force depends on the wave elevation. The higher the surface elevation is, the larger is the magnitude of the force. The uniformly distributed pressure on floats leads to the heave and rotational motion responses.

The pitch mode response is plotted in Fig. 18. Since both Node 1 and Node 2 are well restrained by three linking arms, their pitch responses
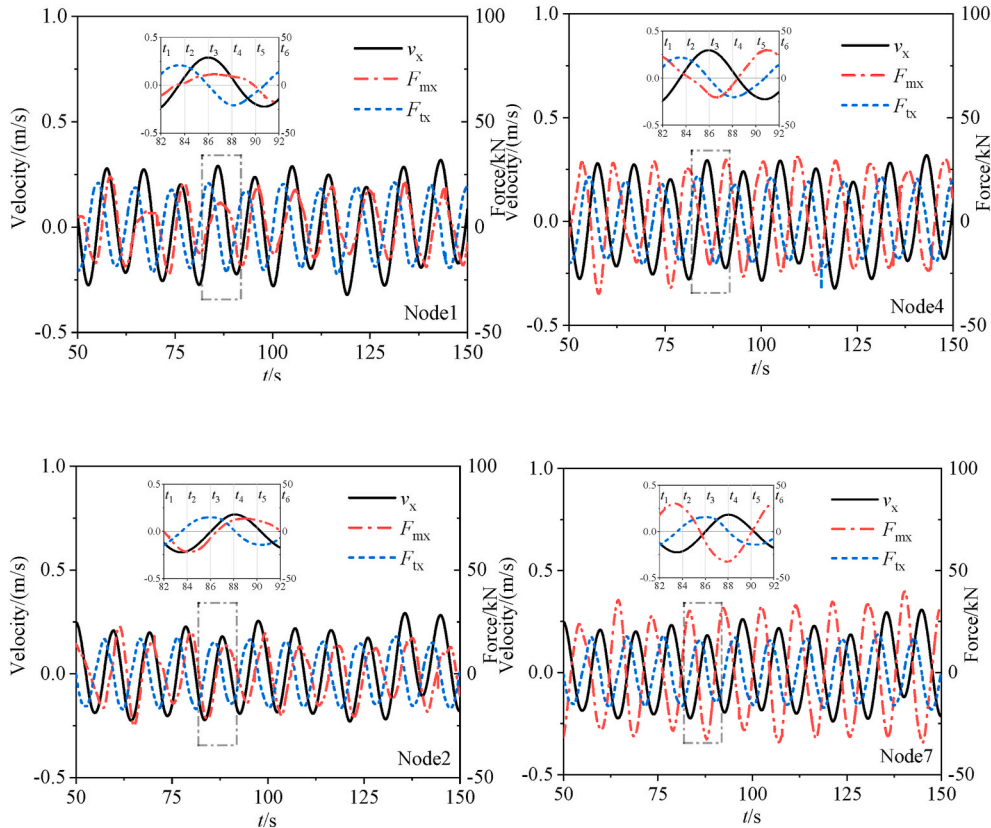

Fig. 15. Velocity v_x, mechanical force F_{mx}, and total forces F_{tx} along the x-axis for each float.
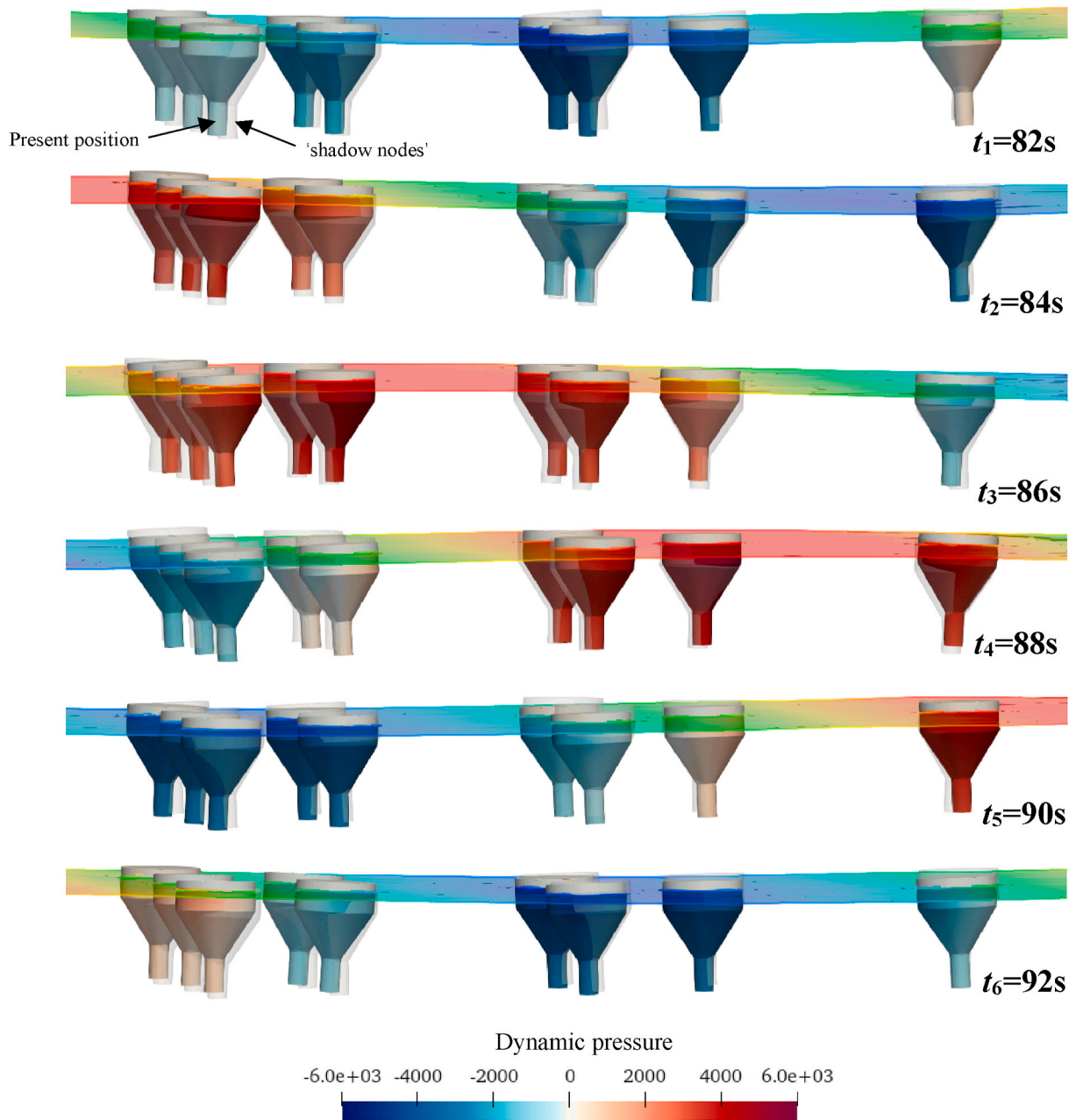
Fig. 17. Free surface around the floats and rotational motion of each float from t_1-t_6.
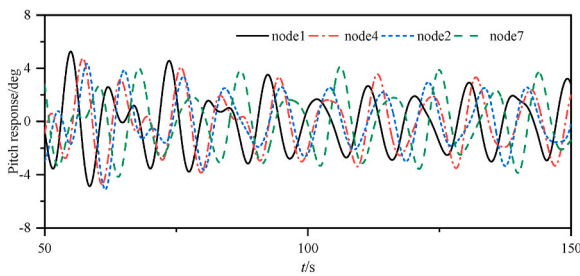

Fig. 18. Time history of pitch mode response for individual float.

are larger than Node 4 and Node 7, for the latter two nodes, the freedom of motion is only constrained by two and one arms, respectively. Fig. 19 summarizes the time-average heave and pitch peak values associated with different wave periods in the present study. It can be seen that the

wave state change has little impact on the time-mean heave response with tested wave frequency, while it influences pitch mode. With a reduction of wave period, closer to the natural frequency of floats, which is 5.1s via experimental test, the wave becomes steeper and the pitch amplitude increases.

5. Discussion

A critical attribute of a WEC system is how much power it can achieve, this will be discussed in this section. This calculation of power output can refer to equations (16) and (17).

Fig. 20 shows the power capture of individual float in the WEC net at a wave condition of $H = 1.5$ m, $T = 9.5$s. It can be seen that the instantaneous peak power capture of individual float varies between 1 and 1.5 kW. Because of their difference in positions in the wave net and the impact received from linking arms, the time-variation of power capture for individual float is not synchronized. This Net&Arm
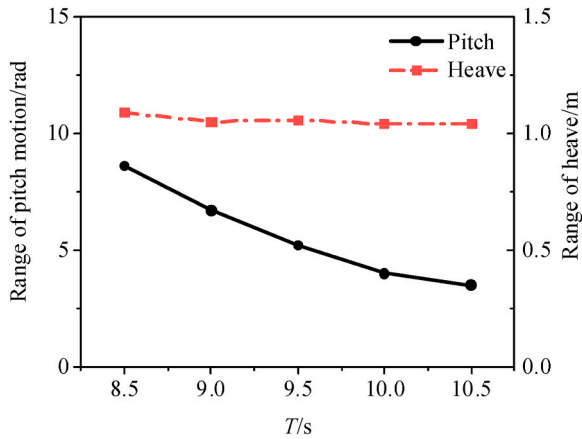
Fig. 19. Time-average pitch and heave amplitude for different wave period.

configuration allows the overall energy output to become more stable. Also, the formation of the net structure reduces the complexity of both device construction and mooring systems. Here, the factors which may influence the power capture are investigated. According to Equations (12) and (13), power capture is controlled by the electric damping and rotational angular velocity, the latter is also influenced by the hydrodynamic force acting on floats.

The influence of electric damping is studied first. Node 2 is selected for the convenience of the study. The time-averaged torque induced by the fluid pressure, the torque due to the electric damping and the angular velocity is presented in Fig. 21. The expected outcome of the study is that the angular velocity decreases with an increase in the electric damping. We also observed that in addition, the hydrodynamic

force increases gradually. When the wave acts on a fixed offshore structure, the induced hydrodynamic force is usually larger than that acting on the same floating structure. The free degree of motion of a floating structure can reduce the hydrodynamic force experienced by it. That's the reason why the torque increases when the float's motion gets weak, as a result of large damping. It can also be observed that both the hydrodynamic and the mechanical torque approach a unified constant when the damping increases once the motion of a WEC is eventually stopped by the large damping. As indicated by Eqs. (17) and (18), the power capture is estimated by velocity and torque. An increase of damping leads to an enlarged torque but a reduced velocity. Therefore, it is reasonable to deduce that an optimal damping should exist to achieve the maximum power capture. This is well reflected in Fig. 21 (b), where this damping is equal to 2000 kN/m.

Except for the electric damping, the hydrodynamic force, which is strongly related to the wave and floating structure interaction, also affects power capture as mentioned earlier. As shown in Fig. 22 (a), the power capture increases dramatically with the decreasing of wave period. Given the same wave period, there's always a peak power capture, however, the matching damping varies with different wave periods. It can be found from Fig. 22(b) that the peak electric damping decreases linearly with wave period. In fact, by shortening wave period from 10.5s to 8.5s, the optimal power capture increases from 4.5 kW to 15 kW.

6. Conclusion

This study aims at developing a coupled CFD-MBD numerical modeling tool to study complicated WEC problems. OpenFOAM is utilized as the fluid solver and a multibody dynamic code is selected to solve structural parts. An adapter is established for exchanging data
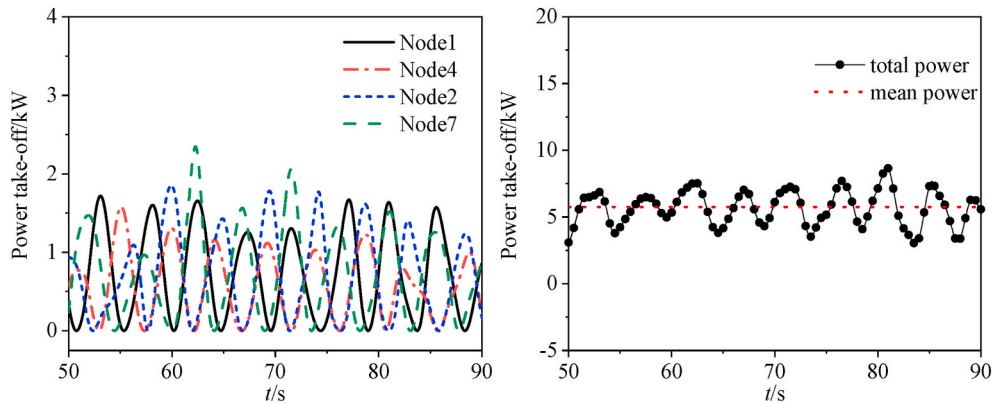

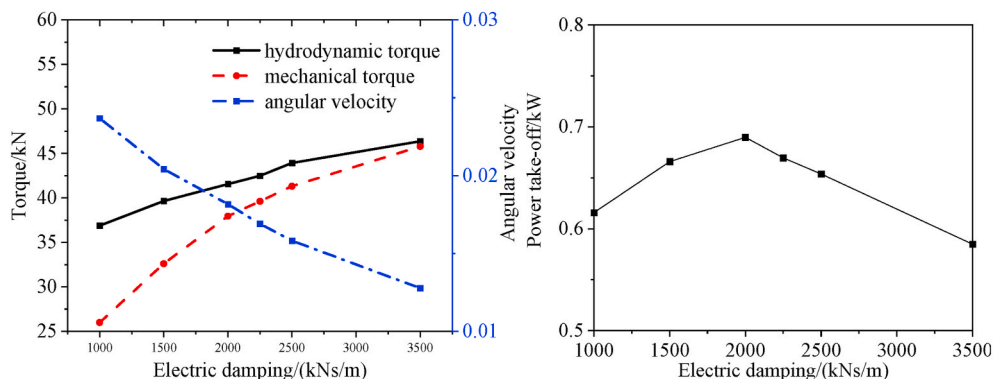**Fig. 20.** Power capture of (a)each float (b)whole system.

Fig. 21. (a)Torque and its angular velocity (b) Power capture with different electric damping of Node 2.
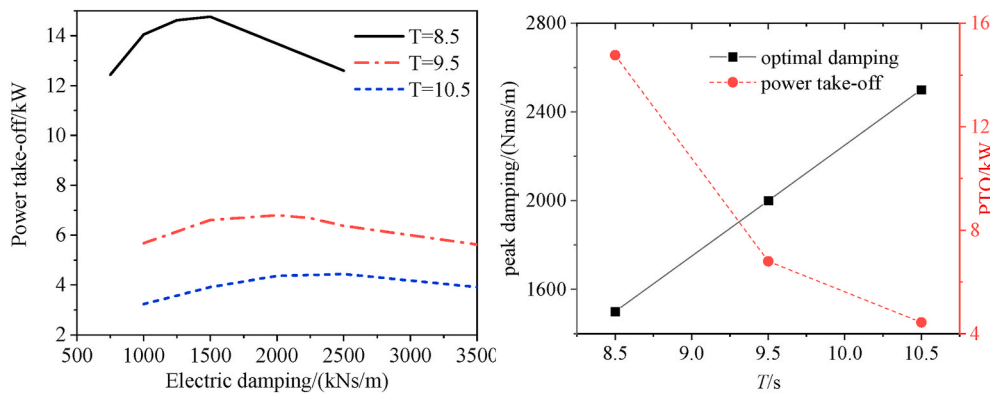
Fig. 22. (a) Power capture under different wave periods (b)Optimal power capture and match damping.

between the above two solvers. The tool is particularly suitable to analyze the WEC net which contains multiple mechanically connected components. Taking Albertan squid WECnet as an exemplar, we demonstrate the success of this integrated numerical modelling tool. In addition, a comparison between the CFD predicted results against nonlinear Morison model results shows that our CFD-MBD framework can better capture high nonlinear effect, which is persistent in the problem associated with a strong wave-structure-interaction. The computational time cost of a nonlinear Morison model study is about 1/10 of that of a CFD simulation. With this tool, a WEC net with 9 floats is examined covering a series of varying wave conditions. We found that the force and moment generated via the connecting mechanical elements, such as the linking arms herein, plays a significant role in the dynamic motion responses of individual float and the WEC net as a whole. The level of such impact also relies on the wave conditions and the specific location of float in the WEC net. By applying electric damping onto the joints, we estimated the device power capture. We found that the power capture damping and wave period are the two most important parameters for the power output. Given a specific wave period, there exists an optimal electric damping force, at which the maximum power can be captured. As expected, the power increases with the decreasing of wave period. For instance, the optimal power capture increases from 4.5 kW to 15 kW when the wave period decreases from 10.5s to 8.5s. This tool has demonstrated its powerful capability to solve such a complex WEC net problem.

However, because of the limitations for handling moving mesh associated with large CFD mesh rotation, it is deemed unsuitable to utilize the existing version numerical tool for a study of a WEC with a very large rotational motion. In addition, cases with short wave periods are not entirely covered in this paper, for which the maximum power capture can be reached as large as 123 kW as estimated in the experiment. To cope with the above problems, further developments will be needed such as using arbitrary mesh interface (AMI) sliding mesh or overset mesh strategy.

CRediT authorship contribution statement

Xiang Li: Conceptualization, Methodology, Software, Data curation, Writing – original draft, preparation. **Qing Xiao:** Conceptualization, Writing – review & editing, Supervision. **Yang Zhou:** Software. **Dezhi Ning:** Writing – review & editing. **Atilla Incecik:** Supervision. **Ryan Nicoll:** Resources. **Anthony McDonald:** Investigation. **David Campbell:** Resources.

Declaration of competing interest

The authors declare that they have no known competing financial interests or personal relationships that could have appeared to influence the work reported in this paper.

References

Agamloh, E.B., Wallace, A.K., Von Jouanne, A., 2008. Application of fluid–structure interaction simulation of an ocean wave energy extraction device. Renew. Energy 33 (4), 748–757.

Albert, A., Berselli, G., Bruzzone, L., Fanghella, P., 2017. Mechanical design and simulation of an onshore four-bar wave energy converter. Renew. Energy 114, 766–774.

Cappietti, L., Simonetti, I., Penchev, V., Penchev, P., 2018. Laboratory tests on an original wave energy converter combining oscillating water column and overtopping devices. In: Proceedings of the 3rd International Conference on Renewable Energies Offshore. RENEW-2018), Lisbon, Portugal2018.

Chandrasekaran, S., Sricharan, V., 2021. Numerical study of bean-float wave energy converter with float number parametrization using WEC-Sim in regular waves with the Levelized Cost of Electricity assessment for Indian sea states. Ocean Eng. 237, 109591.

Chandrasekaran, S., Sricharan, V.V.S., 2020. Numerical analysis of a new multi-body floating wave energy converter with a linear power take-off system. Renew. Energy 159, 250–271.

Chao, Z., Yage, Y., Aiju, C., 2018. Hydrodynamics research of a two-body articulated wave energy device. Ocean Eng. 148, 202–210.

Chen, W., Dolguntseva, I., Savin, A., Zhang, Y., Li, W., Svensson, O., Leijon, M., 2017. Numerical modelling of a point-absorbing wave energy converter in irregular and extreme waves. Appl. Ocean Res. 63, 90–105.

Dang, T.D., Phan, C.B., Ahn, K.K., 2019. Modeling and experimental investigation on performance of a wave energy converter with mechanical power take-off. Int. J. Precis. Eng. Manuf. Green Technol. 6 (4), 751–768.

Davidson, J., Costello, R., 2020. Efficient nonlinear hydrodynamic models for wave energy converter design—a scoping study. J. Mar. Sci. Eng. 8 (1), 35.

Devolder, B., Stratigaki, V., Troch, P., Rauwoens, P., 2018. CFD simulations of floating point absorber wave energy converter arrays subjected to regular waves. Energies 11 (3), 641.

Drew, B., Plummer, A.R., Sahinkaya, M.N., 2009. A Review of Wave Energy Converter Technology. Sage Publications Sage UK, London, England.

Eich-Soellner, E., Führer, C., 1998. Numerical Methods in Multibody Dynamics. Springer.

Finnegan, W., Goggins, J., 2012. Numerical simulation of linear water waves and wave–structure interaction. Ocean Eng. 43, 23–31.

Folley, M., Babarit, A., Child, B., Forehand, D., O'Boyle, L., Silverthorne, K., Spinneken, J., Stratigaki, V., Troch, P., 2012. A review of numerical modelling of wave energy converter arrays. In: International Conference on Offshore Mechanics and Arctic Engineering. American Society of Mechanical Engineers, pp. 535–545.

Ghiringhelli, G.L., Masarati, P., Mantegazza, P., 2000. Multibody implementation of finite volume C beams. AIAA J. 38 (1), 131–138.

Hirt, C.W., Nichols, B.D., 1981. Volume of fluid (VOF) method for the dynamics of free boundaries. J. Comput. Phys. 39 (1), 201–225.

Lawson, M., Yu, Y.-H., Ruehl, K., Michelen, C., 2014. Development and Demonstration of the WEC-Sim Wave Energy Converter Simulation Tool.

Lee, H., Poguluri, S.K., Bae, Y.H., 2018. Performance analysis of multiple wave energy converters placed on a floating platform in the frequency domain. Energies 11 (2), 406.

Liu, Y., Xiao, Q., Incecik, A., Peyrard, C., 2019. Aeroelastic analysis of a floating offshore wind turbine in platform-induced surge motion using a fully coupled CFD-MBD method. Wind Energy 22 (1), 1–20.

Liu, Y., Xiao, Q., Incecik, A., Peyrard, C., Wan, D., 2017a. Establishing a fully coupled CFD analysis tool for floating offshore wind turbines. Renew. Energy 112, 280–301.

Liu, Z., Shi, H., Cui, Y., Kim, K., 2017b. Experimental study on overtopping performance of a circular ramp wave energy converter. Renew. Energy 104, 163–176.

Masarati, P., 2017. MBDyn Input File Format Version 1.7. 3. Politecnico di, Milano.

Masarati, P., Morandini, M., Mantegazza, P., 2014. An Efficient Formulation for General-Purpose Multibody/multiphysics Analysis.

Masarati, P., Sitaraman, J., 2011. Coupled Cfd/multibody Analysis of Nrel Unsteady Aerodynamic Experiment Phase Vi Rotor, 49th AIAA Aerospace Sciences Meeting Including the New Horizons Forum and Aerospace Exposition, p. 153.

Mcdonald, A., Xiao, Q., Forehand, D., Mavel, V., Findlay, D., 2017. Experimental Investigation of Array Effects for a Mechanically Coupled WEC Array, 12th European Wave and Tidal Energy Conference.

Nicoll, R.S., Wood, C.F., Roy, A.e.R., 2012. Comparison of Physical Model Tests with a Time Domain Simulation Model of A Wave Energy Converter. OMAE2012.

Ning, D.-Z., Shi, J., Zou, Q.-P., Teng, B., 2015. Investigation of hydrodynamic performance of an OWC (oscillating water column) wave energy device using a fully nonlinear HOBEM (higher-order boundary element method). Energy 83, 177–188.

Ning, D.-Z., Wang, R.-Q., Zou, Q.-P., Teng, B., 2016. An experimental investigation of hydrodynamics of a fixed OWC Wave Energy Converter. Appl. Energy 168, 636–648.

Ning, D.Z., Zhao, X.L., Chen, L.F., Zhao, M., 2018. Hydrodynamic performance of an array of wave energy converters integrated with a pontoon-type breakwater. Energies 11 (3), 685.

Shabana, A.A., 1997. Flexible multibody dynamics: review of past and recent developments. Multibody Syst. Dyn. 1 (2), 189–222.

Shadman, M., Estefen, S.F., Rodriguez, C.A., Nogueira, I.C., 2018. A geometrical optimization method applied to a heaving point absorber wave energy converter. Renew. Energy 115, 533–546.

So, R., Simmons, A., Brekken, T., Ruehl, K., Michelen, C., 2015. Development of pto-sim: a power performance module for the open-source wave energy converter code wec-sim. In: International Conference on Offshore Mechanics and Arctic Engineering. American Society of Mechanical Engineers. V009T009A032.

Sricharan, V., Chandrasekaran, S., 2021. Time-domain analysis of a bean-shaped multi-body floating wave energy converter with a hydraulic power take-off using WEC-Sim. Energy 223, 119985.

Ticona Rollano, F., Tran, T.T., Yu, Y.-H., García-Medina, G., Yang, Z., 2020. Influence of time and frequency domain wave forcing on the power estimation of a wave energy converter array. J. Mar. Sci. Eng. 8 (3), 171.

Van Rees, W.M., Leonard, A., Pullin, D.I., Koumoutsakos, P., 2011. A comparison of vortex and pseudo-spectral methods for the simulation of periodic vortical flows at high Reynolds numbers. J. Comput. Phys. 230 (8), 2794–2805.

van Rij, J., Yu, Y.-H., McCall, A., Coe, R.G., 2019. Extreme load computational fluid dynamics analysis and verification for a multibody wave energy converter. In: International Conference on Offshore Mechanics and Arctic Engineering. American Society of Mechanical Engineers. V010T009A042.

Wang, L., Robertson, A., Jonkman, J., Yu, Y.-H., Koop, A., Borràs Nadal, A., Li, H., Shi, W., Pinguet, R., Zhou, Y., 2021. Investigation of nonlinear difference-frequency wave excitation on a semisubmersible offshore-wind platform with bichromatic-wave CFD simulations. In: International Conference on Offshore Mechanics and Arctic Engineering. American Society of Mechanical Engineers. V001T001A009.

Yemm, R., Henderson, R., Taylor, C., 2000. The opd pelamis wec: current status and onward programme. In: Proc. 4th European Wave Energy Conference, Alborg Denmark.

Zheng, S., Antonini, A., Zhang, Y., Miles, J., Greaves, D., Zhu, G., Iglesias, G., 2020. Hydrodynamic performance of a multi-Oscillating Water Column (OWC) platform. Appl. Ocean Res. 99, 102168.

Zurkinden, A.S., Ferri, F., Beatty, S., Kofoed, J.P., Kramer, M., 2014. Non-linear numerical modeling and experimental testing of a point absorber wave energy converter. Ocean Eng. 78, 11–21.